Acoustic performance of a large-aperture, seabed, fiber-optic hydrophone array

G. A. Cranch[a)]
SFA Inc., 9315 Largo Drive West, Suite 200, Largo, Maryland 20774

R. Crickmore
QinetiQ, Winfrith Technology Center, Winfrith Newburgh, Dorchester, Dorset, DT2 8XJ, United Kingdom

C. K. Kirkendall
Naval Research Laboratory, Code 5674, 4555 Overlook Avenue SW, Washington, DC 20375

A. Bautista, K. Daley, S. Motley, and J. Salzano
SFA Inc., 9315 Largo Drive West, Suite 200, Largo, Maryland 20774

J. Latchem and P. J. Nash
QinetiQ, Winfrith Technology Centre, Winfrith Newburgh, Dorchester, Dorset, DT2 8XJ, United Kingdom

(Received 24 July 2003; accepted for publication 1 March 2004)

A large-aperture, seabed mounted, fiber-optic hydrophone array has been constructed and characterized. The system is designed for use as a large area surveillance array for deployment in shallow water regions. The underwater portion comprises two arrays of 48 hydrophones separated by a 3 km fiber-optic link, which are connected to a shore station by 40 km of single-mode optical fiber. The hydrophone is based on a fiber-optic Michelson interferometer and the acoustic transduction mechanism is a fiber-wrapped mandrel design. No electrical power is required in the underwater portion. The performance of the system is described, characterized during laboratory measurements and during a recent sea trial. Specifically, measurements of the acoustic resolution, array shape, beam patterns, array gain, and target tracking capability of this array. The system demonstrates self-noise levels up to 20 dB (typically 10 dB) lower than the ambient acoustic noise experienced in the sea trial and array gains close to the theoretical maximum. The system telemetry and electronics have been designed to be expandable to accommodate several hundred hydrophones.
 [DOI: 10.1121/1.1710504]

PACS numbers: 43.30.Wi, 43.30.Yj, 43.38.Zp [RAS] Pages: 2848–2858

I. INTRODUCTION

Optical fiber acoustic sensors are being developed for a variety of passive sonar applications. Since their inception in the late 1970s,[1] this technology has been developed to a level of maturity such that prototype systems have been successfully demonstrated in realistic sea trials.[2] One area of particular interest is shallow water acoustic surveillance. This application requires acoustic arrays comprising in some cases several hundred sensors, which may be located several kilometers from the receiving station. These installations may be deployed for between a few months to several years. For this application the all-optical system offers several advantages. These systems contain no electrical components in the wet-end portion and are therefore light-weight and less susceptible to water ingress, improving reliability. The high multiplexing capability of the optical fiber systems allows several hundred sensors to be interrogated through two fibers or less; requiring only a small diameter cable to link the underwater array to the shore. The underwater portion is also immune to electro-magnetic interference.

Described here is the performance of a large-scale fiber-optic seabed hydrophone array that has been characterized during laboratory tests and during an open water sea-trial. The system comprises 96 hydrophones in total, which are divided into two arrays of 48 hydrophones separated by 3 km. The arrays are designed for conventional plane-wave beamforming. The hydrophones are linearly spaced at 1.51 m intervals, yielding a design frequency, f_d, equal to 488 Hz, where $f_d = c_w/2d$ (here, d is the hydrophone spacing and the sound speed in water, $c_w = 1475$ m/s). Data from the two arrays are processed separately. The arrays are separated by a 3 km fiber-optic cable and connected to the shore by a 40 km fiber-optic link.

The detailed design of this system has been reported elsewhere,[3,4] and emphasis is placed on analyzing the performance of the individual sensors and the array; however, a brief explanation of the operating principle and system design is given in Sec. II. The fiber-optic system contains several different noise sources, compared with electro-ceramic based systems; it is therefore important to accurately characterize each noise source and determine its relative contribution to the total noise. This will allow an accurate prediction of the performance of the system during field use. These noise sources and the correlation of the noise sources between sensors are discussed, followed by the effect on the array detection performance when array beamforming is per-

[a)]Present address: Naval Research Laboratory, Code 5674, 4555 Overlook Avenue SW, Washington, DC 20375; electronic mail: geoff.cranch@nrl.navy.mil

 0001-4966/2004/115(6)/2848/11/$20.00

formed. In Sec. III, measurements of the self-noise of the sensors and data from the field trial are presented. In Sec. IV, the method of determining the array shape after deployment is described and the results are presented. This information is then used to perform shape-corrected conventional beamforming, which allows the beam patterns and array gain to be determined. In Sec. V, the acoustic emission tracking capability of the system is demonstrated. Finally, a summary is given in the concluding section.

II. PRINCIPLE OF OPERATION

A. Background and sensor configuration

A fiber-optic hydrophone operates by converting the acoustically induced strain within an optical fiber placed within the acoustic field into a phase shift in the light propagating in the fiber. This phase shift is converted into intensity modulation by incorporating the fiber into one arm of a fiber-optic interferometer. To enhance the strain induced in the fiber, an amplification mechanism is usually incorporated. The technique used in this system is based on a fiber wrapped air-backed mandrel design.[5] The physical change in the diameter of a plastic mandrel, around which the fiber is wrapped, under the influence of a time varying pressure field induces a strain in the fiber. The air backing increases the compliance of the structure and therefore increases the induced strain within the fiber. An omni-directional hydrophone response is obtained when the acoustic wavelength is much greater than the maximum hydrophone dimension. Multiplexing is achieved by serial concatenation of sensors and using the time of flight of injected optical pulses to sequentially address each sensor. Wavelength division multiplexing is incorporated with the time division multiplexing to permit signals from several time division multiplexed sensor arrays to be combined onto a single optical fiber. Sixteen sensors are multiplexed with time (expandable to 64) and six wavelengths are used to allow 96 hydrophones to be interrogated through two optical fibers. To achieve high phase resolution from the interferometric sensor, a high coherence laser is required that emits a stable single optical frequency. Six erbium doped distributed feedback fiber lasers are used in this system with emission wavelengths ranging from 1541.35 to 1549.32 nm spaced by 1.6 nm. The transfer function of the interferometer is cosinusoidal and therefore an interrogation method is required to linearize the response of the sensor. A heterodyne based method is employed, where by the frequency of the light from each arm of the interferometer is shifted. When the two beams interfere on the detector, a beat frequency equal to the difference in frequency between the two beams is generated. A strain imposed on the fiber will modulate the phase of the light, which will appear as phase modulation sidebands around the beat frequency. The beat frequency is then mixed with a phase locked local oscillator, and the phase information of interest is retrieved using a trigonometric method. A simplified example of a single sensor in this multiplexed configuration is shown in Fig. 1.

The optical emission from the laser is injected into a path-imbalanced interferometer or compensator (COMP). Acousto-optic modulators in each arm frequency shift and

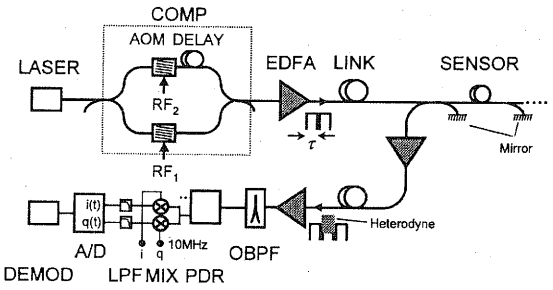

FIG. 1. Sensor configuration.

amplitude modulate the light when driven by a pulsed radio frequency source. The output from one acousto-optic modulator is delayed with a fiber delay line before being combined with the other arm. The compensator thus generates two delayed pulses with a frequency difference, $\Delta f = RF_2 - RF_1$, which are repeated at a frequency, f_{rep}. The pulses are amplified with an erbium doped fiber amplifier (EDFA) and launched into the sensor array. The sensing region of the fiber is defined by splicing two reflective directional couplers at each end. The fiber length in-between the coupler forms one arm of a Michelson interferometer, and is set to give an optical path length equal to half the optical path length of the delay line in the compensator. Therefore, the reflection of the first pulse from the mirror after the sensor arrives back at the detector at the same time as the reflection of the second pulse from the mirror before the sensor. The total phase of this interferometer configuration is the difference in phase between the compensator and the Michelson interferometer sensor,

$$\phi_{\text{tot}} = (2\pi n/\lambda) \cdot (L_{\text{COMP}} - 2L_{\text{MI}}), \tag{1}$$

where n is the effective index of the fiber core, λ is the free-space optical wavelength, and L_{COMP} and L_{MI} are the fiber path imbalances in the compensator and Michelson interferometer, respectively. In the ideal case $(L_{\text{COMP}} - 2L_{\text{MI}}) = 0$ and $\phi_{\text{tot}} = 0$; however, imperfect matching of optical fiber paths and thermally induced fluctuations in the fiber lengths result in a small effective imbalance and hence a nonzero total phase. At the detector, the two pulses reflected from each directional coupler overlap and generate the heterodyne beat frequency. Assuming that equal power is reflected from each directional coupler, then the intensity in the heterodyne pulse is given by

$$I = I_{\text{inc}}(1 + V\cos(2\pi\Delta f t + \phi_s(t))), \tag{2}$$

where I_{inc} is the total mean intensity in the heterodyne pulse and $\phi_s(t)$ is the phase modulation containing the acoustic information. V is a fringe visibility term, ranging from zero to unity, that depends on the relative orientations of the polarization of the light from each interferometer arm. Removing the dc component from Eq. (2) and mixing with in-phase (i) and quadrature (q) components of a stable local oscillator yields

$$i(t) = A\cos(\phi_s(t)), \tag{3a}$$

$$q(t) = A\sin(\phi_s(t)), \tag{3b}$$

TABLE I. Definition of terms.

Parameter	Value	Description
$f_{rep}(=1/T)$	120 kHz	Sensor interrogation rate
τ		Pulse width/sample time
L		Sensor fiber length
$D(=\tau/T)$		Duty cycle
Δf	10 MHz	Heterodyne frequency
f_d	488 Hz	Array design frequency
c_w	1475 m/s	Sound speed in water
d	1.51 m	Hydrophone spacing
λ	1550 nm	Free-space optical wavelength
n	1.465	Effective refractive index of fiber core
ϕ		Optical phase
V		Fringe visibility
RIN		Relative intensity noise
P		Optical power
I		Optical intensity
$S_{\delta P}$		Spectral density
γ_{xy}^2		Ordinary coherence function
G_{xy}		Cross-spectra function
N		Number of sensors

where A is proportional to the fringe visibility, photodiode responsivity, received power, and gain in the mixing process. The signal phase of interest is then obtained by taking the arctangent of the ratio of Eqs. (3b) and (3a). Prior to detection, the pulse train is amplified by a second EDFA. An optical bandpass filter (OBPF) is placed at the output to remove amplified spontaneous emission, generated by the EDFAs, that lies outside the optical bandwidth of the signal interrogating the sensor. The effect of polarization induced signal fading is alleviated with a polarization diversity receiver (PDR), discussed in the following. The two outputs of the PDR are each mixed with the local oscillator, low-pass filtered and digitally sampled (A/D). The phase measurement and tracking is then performed digitally by the demodulator. Phase locking the local oscillator to the oscillators driving the acousto-optic modulators allows the phase of the interferometer to be tracked. Although the phase will drift due to thermally induced fluctuations in the fiber lengths and laser wavelength, these effects are usually very slow, and in most cases very low frequency pressure fluctuations ($\ll$1 Hz) can be resolved.

A third EDFA is located at the output of the sensor array. It is powered with an optical pump signal, at a wavelength of 1480 nm, delivered through a separate fiber and is called a remotely pumped EDFA. The gain provided by this amplifier compensates for signal attenuation in the return fiber, and therefore allows the fiber link to be extended.

The definition of terms and values of various parameters used in this paper are given in Table I.

B. Optical sensor noise sources

A noise source refers to any effect that generates a signal, which is unrelated to the acoustic signal of interest and interferes with its precise measurement. In the remotely interrogated optical hydrophone sensor, there are several optical noise sources that can contribute significantly to the total sensor noise. These are: (i) laser frequency noise, (ii) laser intensity noise, (iii) amplified spontaneous emission noise, and (iv) coherent double Rayleigh scattering noise.[6] Other noise sources, such as optical shot noise, detector noise, oscillator phase noise, single Rayleigh backscattering,[7] fiber thermal noise,[8] and input polarization noise[9] are also present but are generally less significant and will be ignored.

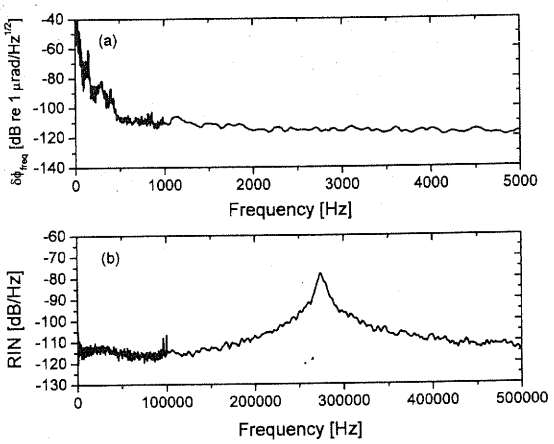

FIG. 2. Laser noise: (a) frequency induced phase noise in a Michelson interferometer with a 1 m fiber path-imbalance and (b) relative intensity noise.

Laser frequency induced phase noise arises from the small path imbalance present in each sensor. An imbalanced interferometer converts input frequency fluctuations into intensity fluctuations, which are proportional to the path imbalance. The frequency induced phase noise, $\delta\phi_{\text{freq}}$, for one laser isolated from environmental noise is shown in Fig. 2(a) scaled to a fiber path-imbalance of 1 m in a Michelson interferometer. Fluctuations in the intensity of the laser also contribute to the sensor noise and generate a noise current on detection indistinguishable from the sensor phase signal. This is characterized in terms of the relative intensity noise spectral density (RIN) where

$$\text{RIN}=\frac{S_{\delta P}}{\bar{P}^2}. \tag{4}$$

$S_{\delta P}$ is the spectral density of the optical power fluctuations and $\bar{P}$ is the mean optical power. A typical RIN spectrum is shown in Fig. 2(b). For the case when the RIN occupies a bandwidth much less than the heterodyne beat frequency, the RIN induced phase noise is given by $\delta\phi_{\text{RIN}}=\sqrt{\text{RIN}}$. RIN appears in the parameter, A, in Eqs. (3a) and (3b) and is therefore common mode to these two signals. Thus, by careful balancing of signal levels during the process of extracting the phase, first-order rejection of the RIN can be achieved. Optical amplifiers in the system generate amplified spontaneous emission (ASE). ASE occupies an optical spectrum approximately 30 nm in width centered on ~1545 nm, most of which is filtered prior to detection. However, ASE noise within the bandwidth of the optical filter (approximately 0.5 nm) will contribute a significant noise source. On detection, two noise contributions arise: noise due to beating of the ASE with the signal, $\delta\phi_{s\text{-}sp}$, and noise due to beating of the ASE with itself, $\delta\phi_{sp\text{-}sp}$. Expressions for these noise sources can be found in Ref. 10 and only their relative mag-

nitudes are considered here. In an optimized system the ASE generated by the remotely pumped amplifier dominates the total noise contribution due to ASE.[10] Coherent double Rayleigh scattering generated in the input fiber also contributes a significant noise source when the input fiber is many kilometers long. This noise source appears as an additional intensity noise and can therefore be reduced by common mode rejection. It is considered here only in terms of the laser RIN.

Finally, another source of noise that has been found to degrade the sensor performance is due to leakage light from the acousto-optic modulators. This is generated when the extinction of the frequency shifted light is not sufficiently high. This continuous leakage light forms multiple imbalanced parasitic interferometers, which generate frequency induced phase noise. In the system presented here the optical extinction ratio of the acousto-optic modulators at the shift frequency is in excess of 100 dB and no degradation in the sensor noise has been observed due to leakage light.

C. Noise in multiplexed systems: Noise aliasing and correlation

The effects of the above-described noise sources are now considered in the case of the multiplexed sensor system. The sensor signals [labeled "$i(t)$" and "$q(t)$" in Fig. 1] consist of a pulse train with each pulse proportional to the function given by Eq. (3a) or (3b). An individual sample is taken during each pulse corresponding to a sample of each sensor. The signal to be sampled contains the phase information of interest as well as noise components that may occupy a bandwidth much greater than the effective sensor sampling frequency, f_{rep}. For the general case of sampling an arbitrary wave form, the Fourier transform of the sampled spectrum is given by the convolution of the Fourier transform of the wave form with the Fourier transform of the sampling function. Consequently, when the wave form occupies a bandwidth greater than the sampling frequency, the components of the wave form at frequencies greater than the sampling frequency will be aliased (or folded) into the true spectrum. The result of this effect can be understood by considering the case of sampling bandwidth limited white noise that occupies a bandwidth much greater than the sampling frequency. In this case, the aliased noise will add incoherently with the spectral components in the true spectrum. This, if bandwidth limited white noise with a power spectral density, $\overline{\eta^2}$, is sampled with a periodic rectangular pulse train of period, T, and pulse width, τ, then the sampled signal will exhibit a noise spectral density equal to $\sqrt{D\eta^2}$, where $D=\tau/T$ is the sampling duty cycle. For bandwidth-limited white noise the effect of aliasing is to increase the noise power in the true spectrum by $\sqrt{D}$. Noise sources such as amplified spontaneous emission noise closely resemble bandwidth-limited white noise and will contribute aliased terms. However, if the spectral density of the noise source decreases for frequencies above the sampling frequency then the aliased noise contribution can be neglected. Conversely, if the noise exhibits a spectral density that increases for frequencies above the sampling frequency, then the aliased noise contribution will be greater than $\sqrt{D}$. This is the case for RIN, shown in Fig. 2(b), which exhibits a noise spectrum resembling an under damped harmonic oscillator.

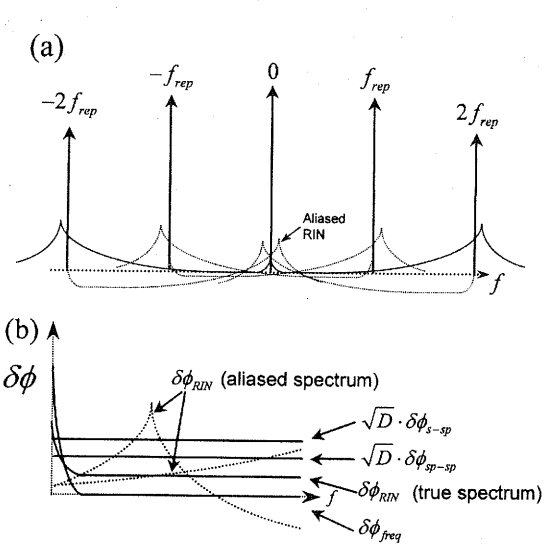

FIG. 3. (a) Fourier spectral content of the signal prior to digitization and (b) sampled spectrum of sensor showing relative levels of noise sources.

Shown in Fig. 3(a) is the convolution of the sampling function with the RIN spectrum, which illustrates the components that are aliased into the true spectrum as dotted lines. The sampling rate is chosen such that the aliased RIN corresponding to the peak in the RIN spectrum (also know as the relaxation oscillation frequency) does not fall within the acoustic bandwidth of the sensor.

The digitized noise spectrum of the sensor therefore comprises contributions from all the noise sources described in Sec. II B and also aliased contributions from the noise sources whose spectral density either remains constant or increase for frequencies above the sampling frequency. The aliased noise contribution cannot be suppressed, since it is not possible to incorporate anti-alias filters prior to the analogue to digital conversion process.

Having determined the significant noise sources in the sensor, it is necessary to consider the effect of noise correlation. Correlated noise may degrade the beamforming process, since the effectiveness of beamforming relies on the implicit assumption that the correlation of the noise between sensors is very low. It is generally valid to assume that the above-described noise sources are statistically unrelated to one another and are therefore uncorrelated. However, optical noise sources that have a common origin, with a weak aliased component, exhibit a high degree of correlation between sensors, particularly at the low frequencies of interest in acoustic sensing. For example, for the case of white noise existing between 0 Hz and f_0 Hz, the degree of correlation of this noise source between two adjacent sensors is given by its normalized autocorrelation function,

$$\hat{R}(\tau)=\sin(2\pi f_0\tau)/(2\pi f_0\tau), \tag{5}$$

where τ is the time between sampling two consecutive sensors. Thus, for the case when $f_0=f_{\text{rep}}/2$ (i.e., the noise bandwidth meets the Nyquist sampling condition) then $\hat{R}(\tau)=0$ (i.e., no correlation) when $\tau=1/(2f_{\text{rep}})$. However, for an

array of N sensors, $\tau \approx 1/(N+1)f_{\text{rep}}$ and in most cases, $\hat{R}(\tau) \neq 0$ (i.e., noise is partially correlated). As the bandwidth of the white noise decreases, then $\hat{R}(\tau)$ tends to unity. This example is also a good approximation for noise sources whose spectral density decreases for frequencies increasing above f_0. In this fiber-optic system, noise sources that fit this criteria are laser frequency noise and double Rayleigh scattering noise. Conversely, when the noise has a strong aliased component the correlation is low, since the aliased noise adds incoherently with the true noise spectrum. This case corresponds to amplified spontaneous emission noise. An example of the relative contributions of the noise sources is illustrated in Fig. 3(b). The exact level of each noise source will depend on the system configuration; however, in most systems of this type the sensor noise will be limited by ASE noise generated by the optical amplifiers.

To quantify the correlation of noise between sensors, the ordinary coherence function, γ^2, is employed, where

$$\gamma_{xy}^2(f) = \frac{G_{xy}(f)F_{xy}^*(f)}{G_{xx}(f)G_{yy}(f)}. \tag{6}$$

Here, G_{xy} is the cross-spectral density between signals x and y, G_{xx} is the power spectral density, and* indicates complex conjugation. This quantity must be calculated by averaging over several records, since for a single average γ_{xy}^2 equals unity. The effect of correlated noise on the array performance is observed when the array data are beamformed. For our analysis, a conventional phase shift and add beamformer is employed. The beamforming process provides an enhancement in signal-to-noise ratio (SNR) in the direction of the acoustic emission, when the array is in an isotropic noise field. The enhancement in SNR is known as the array gain and correlated noise reduces the array gain obtained by the beamforming process, in the broadside direction.

D. Polarization diversity receiver

The visibility term, V, in Eq. (2) includes components for the laser coherence, optical loss, and polarization of the light from each arm of the interferometer. The coherence lengths of the lasers used in this system are several orders of magnitude larger than the differential path mismatch in the Michelson interferometer and this effect can be ignored. The loss component includes the effects of the coupler coefficients, mirror reflectivity, and other optical losses, which can imbalance the return powers from each arm of the interferometer. The intrinsic visibility component resulting from an imbalance in received intensities is given by $V_i = 2\sqrt{I_1 I_2}/(I_1+I_2)$, where I_1 and I_2 are the optical intensities at the detector from arms 1 and 2 of the interferometer, respectively. This establishes the maximum achievable visibility and is effectively set at manufacture of the array with some small thermal and aging related variation. The polarization component of the visibility accounts for the state of polarization (SOP) of the light from each arm of the interferometer. If the polarization states are aligned they will optimally interfere but if they are orthogonal to one another there will be no interference, resulting in what is referred to as a polarization induced fade. This causes an increase in the sensor noise. Without the use of a PDR, the polarization induced visibility component is given by $V_p = \cos(\eta)$ where η is the angle between the two SOPs. Environmentally induced perturbations on the fiber cause the SOP of the light from each arm to vary randomly with time and η can vary between 0 and 90°. Typically this is not acceptable and some method to either eliminate or manage the polarization induced fading must be incorporated.

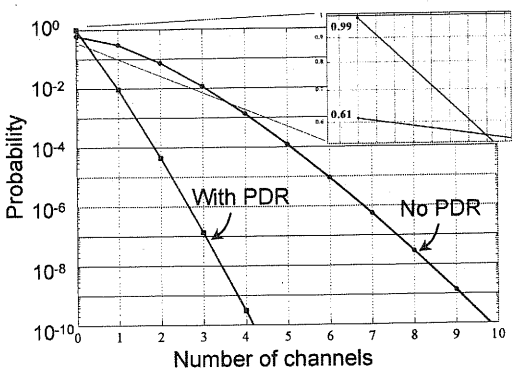

FIG. 4. Probability that N channels of a 48-element array experience a polarization induced signal fade of less than 10% (i.e., $V_p < 0.1$).

The use of a polarizer based PDR is a common technique to overcome polarization induced fading and a "bi-cell" configuration is used in this system. Polarizer-based PDRs interfere the return signal across multiple polarizers with different angular orientations and select the output with the largest interference signal for further processing. Systems incorporating three linear polarizers angularly spaced by 60° can be shown to eliminate the possibility of a complete signal fade.[11] Bi-cell configurations, which incorporate two orthogonal polarizers, do not eliminate the possibility of a complete signal fade but they do significantly reduce the possibility of it occurring to an acceptable level. Figure 4 shows the probability that a given number of channels in a 48-element array have a polarization induced visibility term less than 10% (i.e., $V_p < 0.1$), for both the bi-cell PDR and the no PDR cases. The magnitude of the signal fade that can be accommodated is dependent on the noise and dynamic range of the detector as well as the above-given intrinsic visibility. Referring to Fig. 4, the probability that none of the 48 channels have faded below the 10% level is 99% when the bi-cell PDR is present and 61% when no PDR is present (i.e., 99% of the time, no channels in a 48-element array will have faded below 10% of their maximum value when a bi-cell PDR is used). The probability that two channels have faded below 10% is only 0.004% for the bi-cell PDR. Thus, during an 8 h acquisition one channel will fade by greater that 10% over approximately 5 min and two or more channels will fade for a little more than 1 s. Losing one channel in the array does not seriously degrade performance and is deemed acceptable for this application. The bi-state PDR reduces the electronics and signal processing requirements by one-third, compared to a three polarizer based PDR approach.

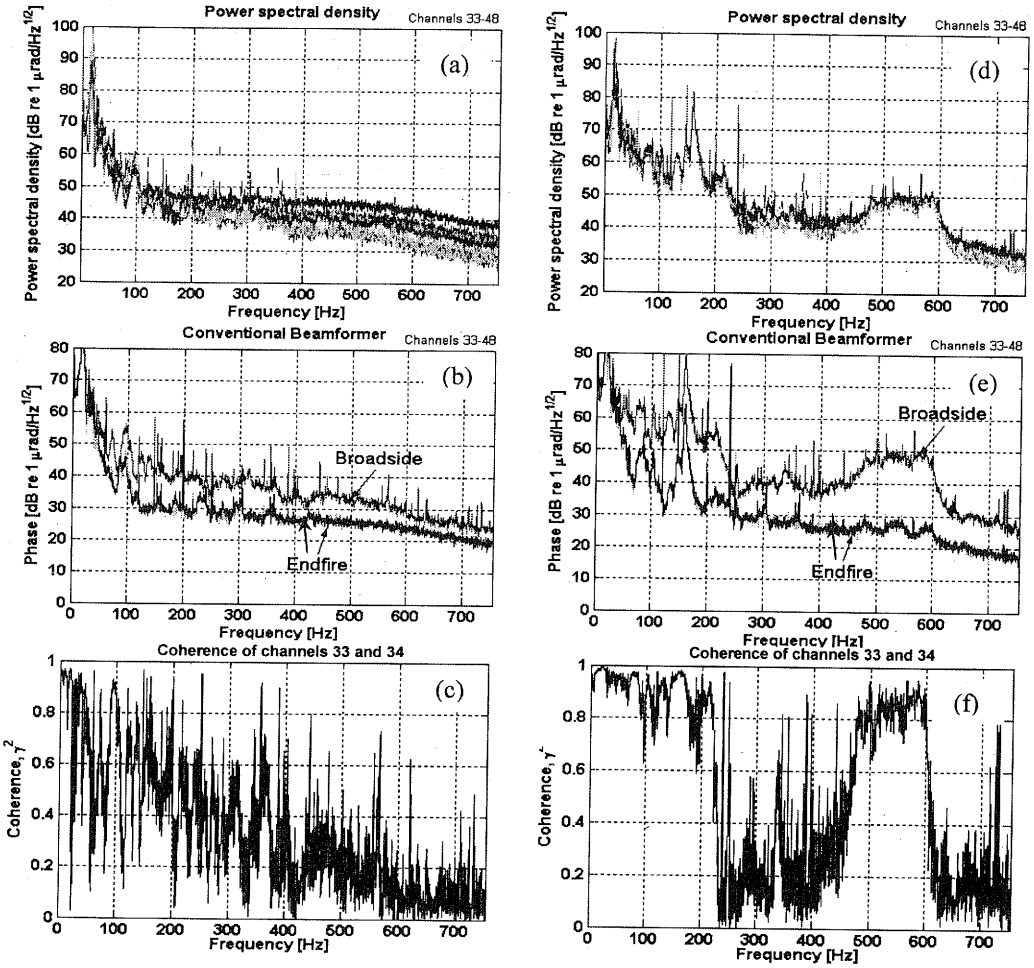

FIG. 5. System self-noise power spectral density, beamformed data, and adjacent channel coherence. Array 1, 35 km link: (a) power spectral density, (b) beamformer, (c) coherence; array 2, 35 km link: (d) power spectral density, (e) beamformer, (f) coherence.

III. SYSTEM PERFORMANCE

A. Laboratory measurements

The system noise is characterized by replacing the hydrophone sensors with a "simulator" array. This consists of 16 sensors arranged in the same in-line Michelson configuration, but with the fiber for each sensor wound onto a piezoceramic (PZT) cylinder. This "simulator" array is placed into an acoustically isolated box. The measured sensor noise is now limited by system noise and not ambient acoustic noise. Driving the PZT cylinders allows signals to be individually injected onto a sensor. During these tests, all six wavelengths interrogated the same simulator array, and thus the self-noise at each wavelength can be directly compared. The phase resolution is expressed in units of dB re 1 μrad/Hz$^{1/2}$ and can be converted to a noise equivalent sound pressure level by subtracting the hydrophone responsivity (−7.5 dB re 1 rad/Pa).

The sampled data are filtered and decimated to yield an acoustic bandwidth of ~750 Hz. The frequency response of the digital filter exhibits a roll-off of ~7 dB for frequencies greater than 500 Hz, which is reflected in the following phase spectra.

The arrays are denoted array 1 and array 2. The phase noise spectral density for sensors 33–48 in arrays 1 and 2 are shown in Figs. 5(a) and (d), respectively, and have been chosen to illustrate best and worst case examples of sensor noise. These measurements were taken with a 35 km fiber link on the input and output. The variation in total noise between the sensors is due to the combined effects of variation in received power from each sensor and polarization induced signal fading. The phase resolution obtained was ~40 dB re 1 μrad/Hz$^{1/2}$ at 500 Hz, which corresponds to a pressure resolution of 47.5 dB re 1 μPa/Hz$^{1/2}$. In both arrays, at frequencies below ~100 Hz, the noise is limited by laser frequency fluctuations. In array 2, a significant elevation in the noise is present for frequencies between 100 and 200 Hz and between 400 and 600 Hz (some narrowband tones originating from the power supplies are also present in the noise spectra). This is due to laser frequency fluctuations induced by the environmental sensitivity of the laser. The packaging in which the lasers used to interrogate array 1 were incorporated provided better isolation to environmental disturbances than that used for the lasers interrogating array 2. The detrimental effect of this laser noise is shown by the beamformed data, which are given in Figs. 5(b) and (e). (These are calculated with a conventional beamformer, a Hann time window, and no aperture shading.) Three beams are shown for each array, corresponding to each endfire direction and broadside. The noise at broadside is greater than the noise at endfire for both arrays; however, the increase in noise is much greater

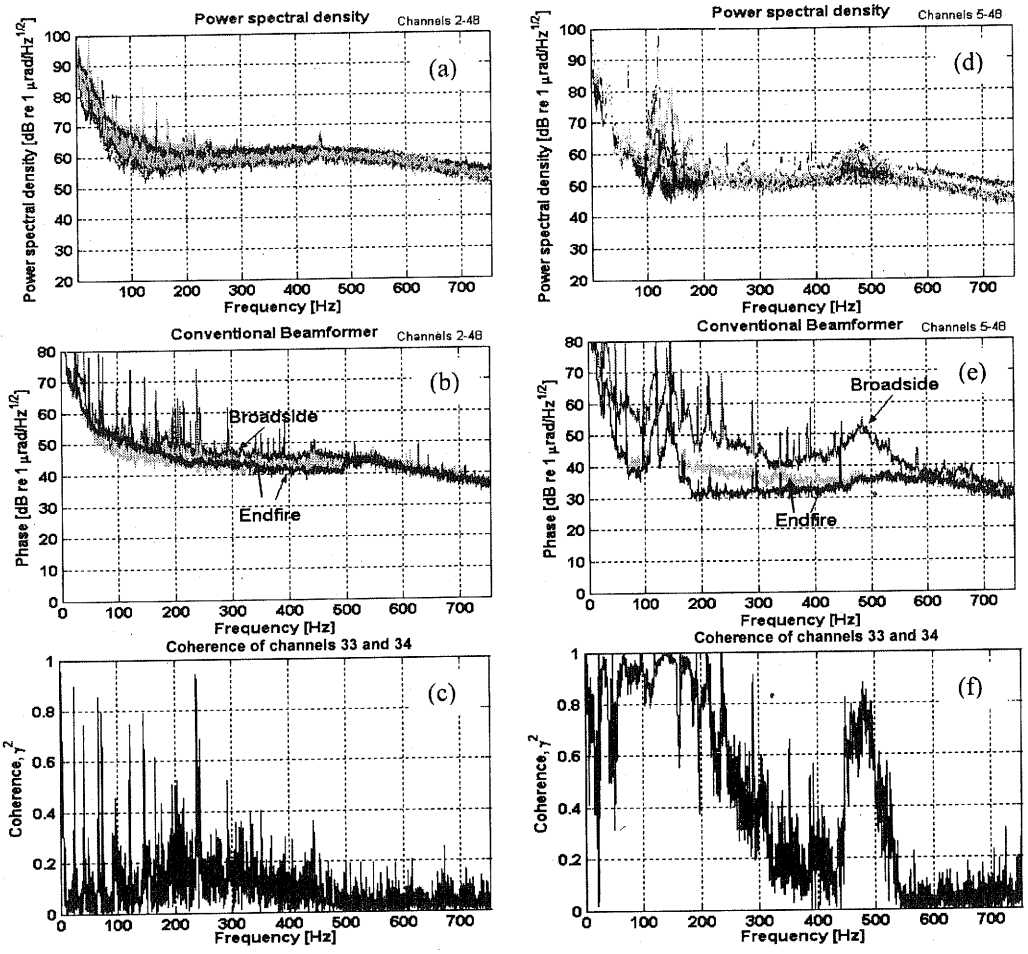

FIG. 6. At-sea ambient noise. Array 1, 35 km link: (a) power spectral density, (b) beamformer, (c) coherence; array 2, 35 km link: (d) power spectral density, (e) beamformer, (f) coherence.

for array 2, particularly at frequencies between 400 and 600 Hz. This shows that the sensor self-noise adds coherently, rather than incoherently, when the data are beamformed in the broadside direction. The correlation between sensor noise is quantified by calculation of the coherence between two adjacent sensors, which is shown in Figs. 5(c) and (f) for arrays 1 and 2, respectively (these plots are typical of the coherence between two adjacent sensors). The coherence is close to unity for frequencies less than 100 Hz for array 1 and frequencies less than 200 Hz and between 500 and 600 Hz for array 2. Consequently, at frequencies where the coherence is high the beamforming process yields little improvement in signal to noise ratio at broadside. In the presence of an incoming acoustic signal at broadside, if the sensor noise is highly correlated and the ambient sea-state induced phase noise is comparable to the sensor self-noise, then the array gain will be significantly degraded. Therefore, the sensor self-noise must be sufficiently lower than the ambient noise to ensure that correlated sensor noise does not degrade the beamforming process.

Injecting narrowband tones onto a single sensor and measuring the signal amplitude on adjacent sensors allows cross-talk to be characterized. This was found to range between −39 and −66 dB at 100 Hz depending on the sensor location relative to the test sensor.

B. Sea-trial measurements

Arrays 1 and 2 were deployed a few kilometers from the coast of a major military and commercial shipping port. A 3 km fiber-optic cable joined each array and a 5 km cable connected array 1 to the shore station. For the majority of the tests, an extra 35 km of optical fiber wound onto spools was added to the input and output fibers, to increase the effective array standoff to 40 km. Array 1 was deployed at a depth of 57 m and array 2 at a depth of 73 m. Shown in Figs. 6(a) and (d) are the phase noise spectral density for all useable channels from data taken during the sea trial. The region where the array was deployed experienced a lot of marine traffic and there were few opportunities when no marine traffic was present. However, these plots represent "quiet" periods and allow the spatial filtering ability of the array to be examined. The ambient acoustic noise at this time was close to sea state 3 for array 1 and sea state 1 for array 2. This results in an ambient acoustic induced phase noise approximately 20 dB higher than the mean sensor self-noise at 488 Hz for array 1 and up to 10 dB higher than the sensor self-noise for array 2 (it is assumed that the environmentally induced laser noise level during the laboratory measurements is similar to that during the sea trial). The beamformed data, calculated with no aperture shading and shown in Figs. 6(b) and (e), demonstrates that for array 1 the noise adds incoherently. Thus,

with an acoustic signal present an array gain of ~15 dB would be obtainable at all steer angles (beamforming the data also reveals a weak target in one of the endfire directions). However, for array 2 the noise is coherent, which results in an increase in the beamformed noise by up to ~15 dB in the broadside direction compared with the endfire directions. The array gain for a 48-hydrophone array with no aperture shading and linear spacing, in an isotropic noise field at the design frequency is given by $10\log_{10}(N)$, which for $N=48$ yields 16.8 dB. Thus, during this data acquisition, close to the maximum array gain would be obtainable from array 1; however, coherent noise from the lasers would degrade the array gain for array 2 in the direction of broadside. The correlation of the noise is confirmed by examining the coherence between two adjacent hydrophones as shown in Figs. 6(c) and (f). The frequencies at which coherent noise addition is observed in array 2 corresponds to regions of high signal coherence, indicating that a highly correlated component is present in the sensor signals. It should be emphasized that the correlated noise level between different sensors in array 2 was found to be rather variable. The data shown here represent a period when the correlation was above average.

IV. ARRAY BEAM PATTERNS AND ARRAY GAIN

A. Shape measurement

During the deployment procedure the aim is to lay the hydrophones in a straight line with no slack in the cable between them. Although the arrays were deployed under tension as they entered the sea, the effect of ocean currents at various depths can affect how the array is deposited onto the sea bottom. Therefore, measurements must be performed to determine the actual positions of the hydrophones within each array.

These experiments were conducted by deploying an acoustic source at eight different positions around each array. At each position chirp signals were transmitted across the band 50–2000 Hz. The length of the chirp was 2 s and it was repeated continuously over a period of about 1 min. The Global Positioning System (GPS) data of the boat from which the source was deployed were recorded at the start and end of the chirp transmissions.

The hydrophone locations are calculated using the following procedure: replica correlation functions are calculated between the transmitted signal and the received signals for each of the hydrophones in the array. Relative travel times are then calculated between the sensors from the correlation data for each of the propagating paths. A propagation model is used to predict relative travel times for each path. Sensor and source positions are determined by minimizing the residual error between the measured and modeled delays using a technique similar to that described in Ref. 12. When calculating the delays, a sound speed equal to 1475 m/s at all depths is assumed.

The inverse problem of estimating sensor positions from time delay information is nonunique and ill conditioned. An iterative linearized inversion is employed, which determines the optimum solution by including *a priori* information about the problem. A two-stage process has been adopted to determine the positions of the sensors and sources. In the first stage an optimization procedure is performed to determine the absolute location of the array (relative to the nominal source positions). To achieve this, the positions of the sources are fixed at their nominal positions obtained from the GPS measurements made during deployment. The depths of the sensors are also fixed at their initial positions (interpolated from the water depth at the array). In the second stage, a further inversion procedure is performed to determine the optimum positions and depths of both the sensors and sources. In the second inversion, the position of sensor 24 in the array is fixed and the positions of the remaining sensors relative to it are determined.

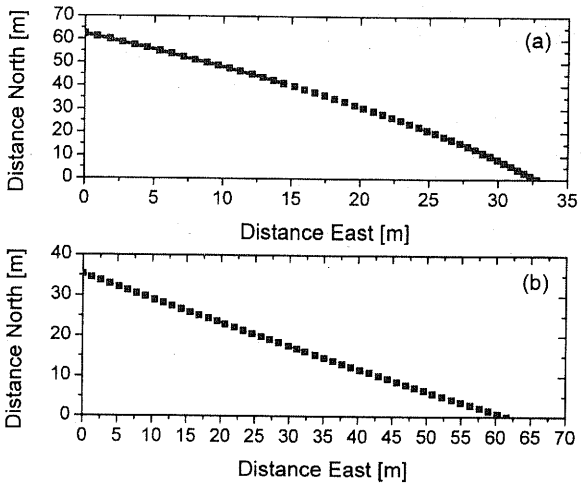

FIG. 7. Derived shape of (a) array 1 and (b) array 2.

Figures 7(a) and (b) show the derived shapes for the two arrays. Array 1 is slightly curved, with the headings at each end of the array differing by 17°. Array 2 is much straighter with the heading at each end differing by only 4°. The curvature of array 1 is beneficial and will be utilized to resolve the left/right ambiguity in the beam pattern.

B. Beam patterns and sidelobe suppression

In order to test the beamforming capabilities of the array, measurements are made using a signal transmitted by an acoustic source towed behind a surface ship. For these experiments, the signal consisted of broadband noise and a number of tonals at known frequencies. In order to track the towed source it is necessary to beamform the data. This has been done using a conventional shape corrected beamformer with the hydrophone positions obtained from the hydrophone localization measurements. For the following data analysis, a Hann window is used in the temporal domain, while in the spatial domain a Kaiser–Bessel window is used, designed to give a maximum side lobe suppression of −36 dB.

An important feature of a hydrophone array is the level of the sidelobes in the beam pattern, which affects the ability of a system to detect a weak signal in the presence of a larger one on a different bearing. Beam patterns at 445 Hz for both arrays have been calculated at a time when the towed source was relatively close to the arrays and so there was a strong signal from a particular direction. For a perfectly straight array an acoustic signal arriving on opposite sides of the

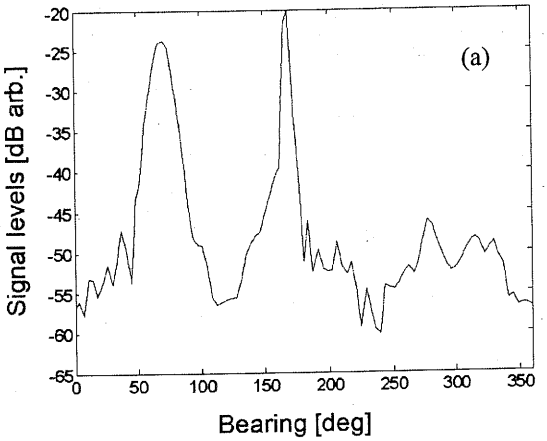

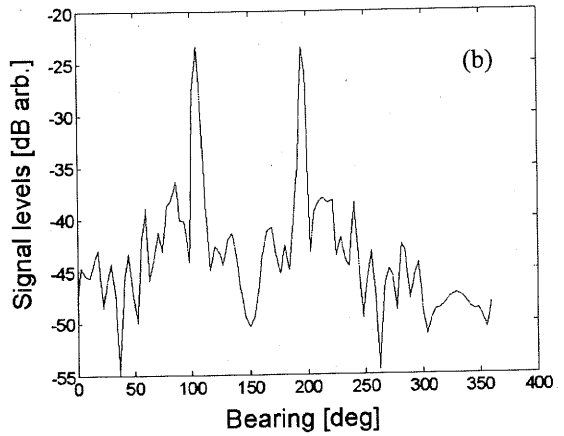

FIG. 8. Beam pattern for (a) array 1 and (b) array 2.

array but at the same angle to broadside, will result in exactly the same phase differences between the signals detected by each hydrophone. It would therefore not be possible to determine which was the actual direction of arrival and this effect is known as the left/right ambiguity. Figure 8(a) shows the beam pattern from array 1 for a towed source range of 1.0 km on a bearing of 170°. The main peaks are at the true bearing and the corresponding bearing on the other side of the array. The curvature in this array results in the peak at the true bearing being sharper and higher than the false one, thus allowing the left/right ambiguity to be resolved. The highest sidelobe is ~26 dB lower than the main peak. A similar ratio is obtained at a latter time when the towed source is at a range of 4.7 km and the signal is 17 dB lower. This suggests that the sidelobe level is determined by leakage from the main peak rather than the background noise level. The array shading used in the beam pattern should give a maximum sidelobe level of −36 dB for a straight array. The higher sidelobe level is partly due to the array curvature, and partly to a number of other effects including variation in responsivity of the hydrophones, and errors in their calculated positions.

Figure 8(b) shows the beam pattern for array 2 when the towed source was at a range of 2.3 km and a bearing of 195°. Due to the straightness of this array, the two peaks are almost identical and it cannot be determined from the beam pattern which peak corresponds to the true bearing. The maximum sidelobe level in this case is only ~15 dB below the main peak although they are lower at greater separations from the peak.

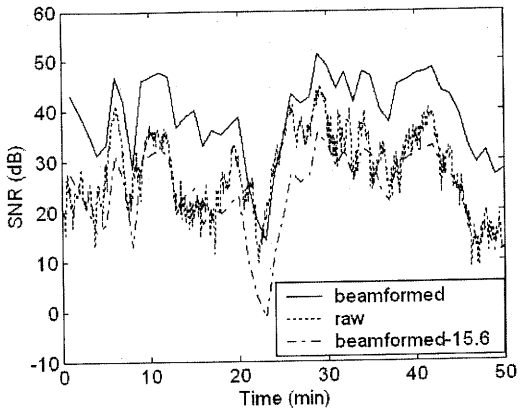

FIG. 9. SNRs of beamformed and raw data.

The sidelobe suppression in array 2 is expected to be lower than array 1 since four of the hydrophones were damaged during manufacture of the array and produced no acoustic signal. To try and minimize the effect of this missing data on the beam pattern, the analysis program estimates the missing hydrophone signal by interpolating values from the remaining hydrophones. However, the interpolation cannot perfectly reconstruct the missing data and the errors introduced by the interpolation have the effect of increasing the sidelobe levels. It may also be the case that the hydrophone responsivity is more variable in array 2 or that the errors in the calculated hydrophone positions are greater than estimated.

In order to compare the width of the peak in the beam pattern with the predicted value, the same beamforming procedure is used to process ideal simulated data. The simulated data corresponds to a signal of 445 Hz incident on a straight array with the same number of hydrophones and spacing. Although, due to its idealized nature, the sidelobe levels are lower for the simulated data, it is found that the width of the two peaks down to 20 dB below their maxima is very similar. This demonstrates that any variation between the hydrophone responsivities and uncertainties in their positions do not adversely affect the width of the peak.

C. Array gain

As discussed earlier, the gain of an array is defined as the increase in the SNR that is obtained by beamforming in the direction of the source. To demonstrate this effect the SNR of the signal at 445 Hz is used, this being defined as the ratio between the 445 Hz signal and the mean noise level in the frequency bands within 50 Hz on either side of the peak.

The SNRs, which are shown in Fig. 9, have been calculated with 50 min of data collected by array 1. To obtain the SNR from the raw data, the power spectrum from each hydrophone in the array is calculated followed by the mean value over all hydrophones. Since the mean is calculated using the power spectrums, the phase information of the hydrophones is lost and no increase occurs in the SNR when the signals from all the hydrophones are combined. For the

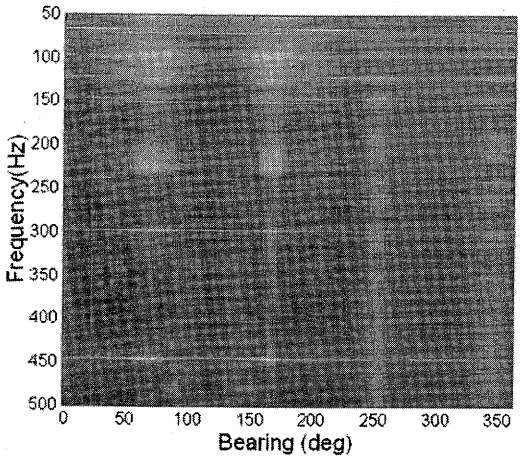

FIG. 10. Beam pattern image of towed source.

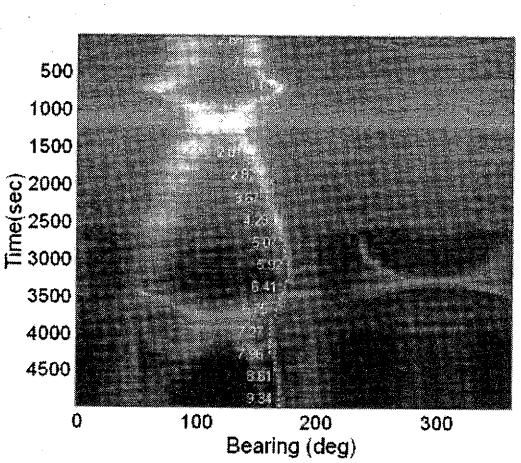

FIG. 11. Tracking pattern using array 1 data.

beamformed data the SNR is calculated using the frequency spectrum of the beam in the direction of the towed source.

The predicted value of the array gain depends on the number of hydrophones in the array and the weighting function used in the beamforming, and for this configuration is 15.6 dB. The dot-dash line in Fig. 9 shows the beamformed SNR minus 15.6 dB, which if the array gain is as predicted should overlap with the dotted line showing the raw SNR. Although there is short term variability in the two lines their general levels agree, showing that the array can achieve the predicted gain. The main discrepancy is between 20 and 30 min and this is due to the nature of the noise in this period. The calculation of the array gain assumes that the noise on each hydrophone is isotropic; however, inspection of the data between 20 and 30 min shows that the noise mainly originates from the ship towing the towed source, which during this period was quite close to the array. Under these circumstances the array gain should be less than the optimum value, which is the situation that is observed.

V. ACOUSTIC EMISSION TRACKING

Figure 10 shows the results of beamforming data from array 1 during one of the towed source runs, when the source was at a bearing of 168°. The gray scale shows the amplitude of the signal as a function of bearing and frequency. The strongest signals occur at both the true bearing and at 80°, which would be a signal arriving at the same angle to broadside but from the other side of the array. Again, the true bearing is higher and has a smaller angular width than the false one and so the left–right ambiguity can be resolved. As well as the vessel with the towed source there also appears to be a second vessel present on a bearing of 255°, which accounts for the broadband signal at that bearing and the "mirrored" signal at 340°. The presence of coherent noise in the array would generate an apparent signal at the two broadside directions of 26° and 206°. The lack of any such signal demonstrates that the coherent noise is low enough not to have any observable effect.

The towed source transmitted a number of discrete frequencies and since the angular resolution of an array increases with frequency, tracking is most accurately achieved using the highest of the discrete frequencies, which is 445 Hz. To show the capability of the system to track the towed source only the section of the beam pattern at 445 Hz is used, and this is combined with the same section from subsequent beam patterns. This enables an image to be created that shows how the bearing and strength of the signal at 445 Hz varies as the towed source moves. Such an image, shown in Fig. 11, has been created from 4900 s of data from array 1.

At times up to 2500 s the strongest signal detected is from the towed source; however, as it moves further away its signal strength decreases and the signal from another nearby vessel becomes higher.

As before there are normally two maxima on the trace due to the left/right ambiguity. When the towed source moves near the endfire position (which happens around 1200 s), the angular resolution of the beam pattern becomes worse and the two traces merge. The right-hand trace is narrower and more intense, which shows that this represents the true bearing. The dotted white line in this figure shows the actual bearing of the towed source calculated from the log of its GPS positions. The numbers beside this line show the range in kilometers of the towed source from the array at that time. There is clearly very good agreement between the actual and measured bearing out to a range of around 5.5 km (3000 s) after which time the signal from another vessel temporarily masks the signal from the towed source. After 4200 s, when the other vessel has moved away, there is still a faint trace that follows the dotted line, which shows that the towed source is being detected to a range of ~9 km.

VI. CONCLUSIONS

This paper describes the design and acoustic performance of a large-aperture, seabed mounted, fiber-optic hydrophone array. The system comprises two arrays of 48 hydrophones separated by a 3 km fiber-optic link, which are connected to the interrogation electronics at a shore station through 40 km of optical fiber. The sensors are multiplexed using time and dense wavelength division multiplexing. An erbium doped fiber amplifier is incorporated into the underwater array, which is optically powered by a pump laser located within the interrogation electronics. The system has been characterized by tests carried out in the laboratory and during a sea-trial. During the sea-trial, the array was de-

ployed a few miles from the coast of a major military and commercial port. The portion of the array deployed in the sea is entirely passive and requires no electrical power. The hydrophones in the array are linearly spaced at 1.51 m intervals. An element localization method has been used to determine the shape of the array after deployment. Processing the acoustic data with a shape corrected conventional beamformer has demonstrated successful tracking of a towed acoustic source by a surface vessel. Other passing vessels can also be simultaneously tracked. The width of the main lobe in the beam patterns and the array gain achieved agrees with the theoretically predicted values. One of the arrays was laid on the seabed with a small amount of curvature. This has enabled the left–right ambiguity in the bearing of a target, which exists for a perfectly straight array, to be resolved.

The ambient acoustic noise measured with the arrays on the seabed is typically 10 dB higher than that measured in the laboratory, thus the sensor noise is generally limited by ambient acoustic noise. Correlation of the noise between sensors has been characterized. The noise correlation for sensors interrogated by the same laser is generally higher than between sensors interrogated by different lasers and is found to be due to the environmental sensitivity of the lasers. Isolation of the lasers from environmental noise greatly reduces this noise correlation.

The optical architecture permits the number of multiplexed hydrophones to be significantly increased without increasing the number of optical fibers in the link cable. Thus, this system is suitable as a rapidly deployable, large-area surveillance array.

ACKNOWLEDGMENTS

This work was carried out as part of a collaboration between the Naval Research Laboratory, U.S. and Defense Science and Technology Laboratory, U.K. This project was funded by the US Office of Naval Research, Naval International Programs Office and the U.K. Ministry of Defense. The authors would like to gratefully acknowledge N. Goddard (QinetiQ) for calculating the array shapes and thank G. Cogdell (NRL) for assistance in arranging this collaboration. QinetiQ, UK and Cogent Defense Systems, UK designed and constructed the underwater portion of this system.

[1] J. A. Bucaro, N. Lagakos, J. Cole, and T. Giallorenzi, "Fiber optic acoustic transduction," Phys. Acoust. **XVI**, 385–457 (1982).
[2] A. Dandridge, "Fiber-optic sensors for acoustic array applications," J. Acoust. Soc. Am. **102**, 3168 (1997).
[3] G. A. Cranch, C. K. Kirkendall, K. Daley, S. Motley, A. Bautista, J. Salzano, P. J. Nash, J. Latchem, and R. Crickmore, "Large-scale, remotely pumped and interrogated fiber-optic interferometric sensor array," IEEE Photonics Technol. Lett. **15**, 1579–1581 (2003).
[4] G. A. Cranch and P. J. Nash, "Large-scale arrays of fiber-optic interferometric sensors using TDM and DWDM," IEEE J. Light. Tech. **19**, 697–699 (2001).
[5] P. J. Nash and J. Keen, "Design and construction of practical optical fibre hydrophones," Proc. Inst. of Acoustics **12**, 201–212 (1990).
[6] G. A. Cranch, A. Dandridge, and C. K. Kirkendall, "Suppression of double Rayleigh scattering induced excess noise in remotely interrogated fiber-optic interferometric sensors," IEEE Photonics Technol. Lett. **15**, 1582–1584 (2003).
[7] M. J. Marrone, A. D. Kersey, C. A. Villarruel, C. K. Kirkendall, and A. Dandridge, "Elimination of coherent Rayleigh backscatter induced noise in fibre Michelson interferometers," Electron. Lett. **28**, 1803–1804 (1992).
[8] K. H. Wanser, "Fundamental phase noise limit in optical fibers due to temperature fluctuations," Electron. Lett. **28**, 53–54 (1992).
[9] A. D. Kersey, M. J. Marrone, and A. Dandridge, "Observation of input-polarization-induced phase noise in interferometric fiber-optic sensors," Opt. Lett. **13**, 847–849 (1988).
[10] G. A. Cranch, P. J. Nash, and C. K. Kirkendall, "Large-scale remotely interrogated arrays of fiber-optic interferometric sensors for underwater acoustic applications," IEEE Sensors J. **3**, 19–30 (2003).
[11] N. J. Frigo, A. Dandridge, and A. B. Tveten, "Technique for elimination of polarization fading in fiber interferometers," Electron. Lett. **20**, 319–320 (1984).
[12] S. E. Dosso, B. J. Sotirin, and J. L. Newton, "Array element localization for horizontal arrays via Occam's inversion," J. Acoust. Soc. Am. **104**, 846 (1998).